Supplementary Information

for

Oriented proton-conductive nano-sponge-facilitated polymer electrolyte membranes

Xin Liu+,[a] Junfeng Zhang+,[a] Chenyang Zheng,[a] Jiandang Xue,[a] Tong Huang,[a] Yan Yin,*[a,b] Yanzhou Qin,[a] Kui Jiao,[a] Qing Du,[a] and Michael D. Guiver*[a,c]

[a] *State Key Laboratory of Engines, Tianjin University, Tianjin 300072, China*

[b] *State Key Laboratory of Separation Membranes and Membrane Processes, Tianjin Polytechnic University, Tianjin 300387, China*

[c] *Collaborative Innovation Center of Chemical Science and Engineering (Tianjin), Tianjin 300072, China*

+ These authors contributed equally to this work.

Supplementary Note 1. Abbreviations in alphabetical order.

BET: Brunauer-Emmett-Teller

CP4VP: ferrocyano-coordinated poly(4-vinylpyridine)

DLS: dynamic light scattering

DMF: dimethylformamide

DOE: Department of Energy

DSC: differential scanning calorimetry

DVS: dynamic vapor sorption

EELS: electron energy loss spectrometer

FTIR: Fourier transform infrared spectra

IP: in-plane

MEA: membrane-electrode-assembly

MM: magnetic-cast membranes

NM: normal-cast membranes

NMR: nuclear magnetic resonance

PALS: positron annihilation lifetime spectra

PBA: Prussian blue analogue

PC: proton-conducting component

PEM: proton exchange membrane

PEMFC: proton exchange membrane fuel cell

PSf: polysulfone

PTFE: polytetrafluoroethylene

PWA: phosphotungstic acid

P4VP: poly(4-vinylpyridine)

RH: relative humidity

SEM: scanning electron microscope

SPCAF: sodium pentacyanoammineferroate (II)

TEM: transmission electron microscope

TGA: thermogravimetric analysis

TP: through-plane

UV-Vis: ultraviolet-visible

VSM: vibrating sample magnetometer

XPS: X-ray photoelectron spectroscopy

XRD: X-ray diffraction

15-crown-5: 1,4,7,10,13-pentaoxacyclopentadecane

Supplementary Note 2. Formation of magnetic induced interaction in MMs

After membrane casting, NMs maintain the original green-yellow coloration, which derives from the CP4VP component, but MMs have a blue coloration. Fig. S1a compares the UV-Vis spectra of the original membrane materials, CP4VP, PWA and PSf, which have absorbance maxima at 360 nm, 253 nm and 298 nm, respectively. The wide absorption region of CP4VP around 360 nm extends beyond 400 nm, so that visible purple light (400 ~ 450 nm) is absorbed, giving the green-yellow coloration of CP4VP. The absorption regions of the colorless components PWA and PSf are outside the visible range (400 ~ 700 nm). For the NMs composed of these components, all the absorption spectra correlate with the original materials. In contrast, MMs present a new, very broad and strong absorption around 617 nm, which encompasses the area for yellow and orange light (580 ~ 650 nm), thus giving the MMs a blue coloration. When membranes are acidified in 1 M HCl or soaked in water at room temperature, NMs and MMs exhibit another distinction. All NMs are partially dissolved, imparting a green-yellow color to the water, but MMs maintain their original shape, without any visible leaching out of color. UV-Vis tests for the membrane soaking liquids are carried out to detect solute, as shown in Fig. S1b. Aqueous solutions of CP4VP and PWA display absorbances at 364 nm and 261 nm, respectively. The slight shifts between the absorbances of CP4VP or PWA in the solid (Fig. S1a) and dissolved (Fig. S1b) states may be attributed to the solvation effect of water. Only the NMs show evidence of CP4VP and PWA leaching from the PSf matrix, while the MMs exhibit no extraneous absorbance, reflecting the water insolubility of MMs.

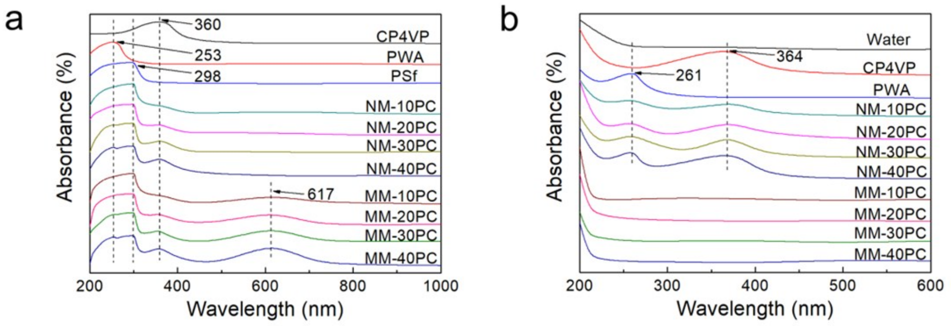

Fig. S1 (a) Solid UV-Vis absorption spectra of CP4VP (powder), PWA (powder), PSf (membrane), NMs (membrane) and MMs (membrane). The new absorbance at around 617 nm in MMs results in their blue appearance and indicates a magnetic field-induced chemical transformation. (b) Liquid UV-Vis absorption spectra of pure water, CP4VP solution, PWA solution, and the leaching liquids of NMs and MMs. Neither CP4VP nor PWA shows evidence of leaching from MMs, suggesting a magnetic field-induced stabilization of the soluble membrane components.

Alterations in the color and solubility of MMs indicate that a chemical transformation beyond simple mixing of the membrane components occurs during magnetic field-assisted casting. To better understand these phenomena, XPS and FTIR are carried out to investigate detailed variations in the membranes. Fig. S2 displays the XPS narrow scans of N and W elements for CP4VP, PWA, NMs and MMs. Fig. S2a shows that the N1s peaks in NMs are at the same positions as CP4VP for both the Fe-pyridine and the cyano ligands, while for the MMs, only the Fe-pyridine part is the same. Marked positive shifts for the N1s binding energy of the cyano ligands are indicative of a reduction in electron density. In contrast, Fig. S2b shows that the W4f peaks of NMs are at the same as that of PWA, but those of MMs show marked negative shifts in binding energy, indicating increased electron density on tungsten. This suggests a transfer of electron density from cyano ligands to tungsten atoms, Similar behavior of shifts occurring for MMs, but not for NMs, are also observed in the comparative FTIR spectra shown in Fig. S3. The cyano absorption bands show a red shift for MMs (Fig. S3a), and the absorption bands related to W−O/W−O−W show a blue shift (Fig. S3b). These results suggest that, under the 35 tesla magnetic field, a new chemical interaction occurs between the N of the cyano ligand in CP4VP and the W in PWA, stabilizing the components in MMs.

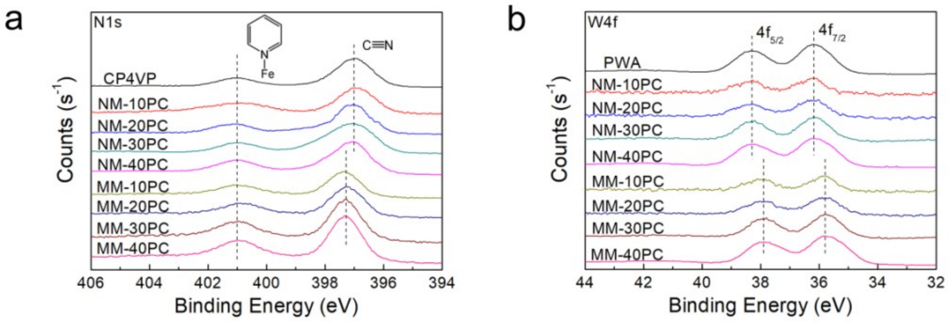

Fig. S2 XPS narrow scans of (a) N1s for CP4VP, NMs and MMs (b) W4f for PWA, NMs and MMs. The opposite shifts in MMs for the binding energies of the N in cyano ligands and the W in PWA indicate electron transfer from N to W, that is, the formation of Fe−C≡N−W bonds.

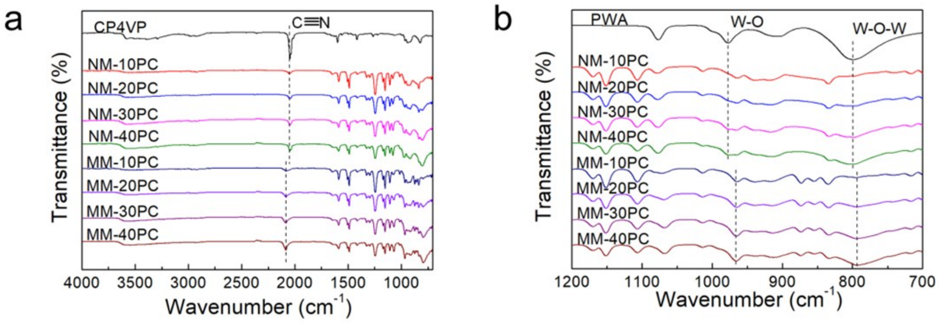

Fig. S3 Comparative attenuated total reflectance FTIR of CP4VP, PWA, NMs and MMs for (a) cyano ligand and (b) W−O/W−O−W group. The opposite shifts in MMs for the absorbance peaks of cyano ligands and W−O/W−O−W groups indicate electron transfer from N to W, that is, the formation of Fe−C≡N−W bonds.

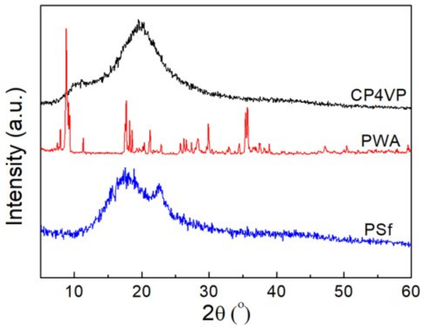

Fig. S4 X-ray diffraction (XRD) curves of original membrane components CP4VP, PWA and PSf.

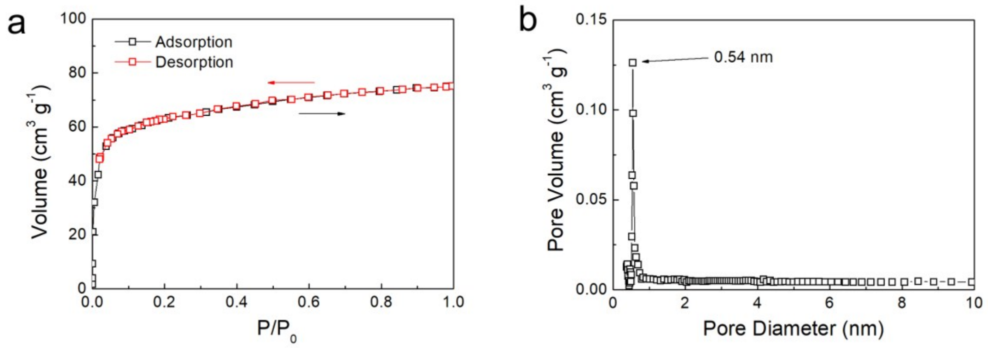

Fig. S5 Brunauer-Emmett-Teller (BET) measurement of a MM-70PC[a] sample. (a) N_2 physical adsorption-desorption curves. The adsorbed volume shows a sharp increase at very low relative pressure, which changes to a gentle slope until the maximum relative pressure is reached. The adsorption and desorption curves are almost identical, showing no hysteresis. This behavior is symptomatic of a material containing only micropores. (b) Pore size distribution estimated by nonlocal density functional theory. Only one peak is obtained, reflecting a pore diameter of 0.54 nm (5.4 Å). The BET results for pore diameter are in agreement with the PALS analysis.

[a] BET measurements to estimate microporosity cannot be obtained for all NMs and MMs with PC loadings of 0~40 wt%. The most likely reason is that the PSf matrix encompassing the microporous PBA hinders the ingress of N_2. While the PSf matrix is found to also possess micropores in PALS analysis (Fig. 2b), the pores in such tough and amorphous polymer are largely unconnected, and therefore not feasible for BET detection. To circumvent this, we prepared an alternative MM-70PC sample with high PC loading. Although intact MMs with PC loading higher than 45% could not be obtained due to poor mechanical properties, one fragment of MM-70PC was

suitable for BET analysis (Fig. S5), as it showed good repeatability compared with MMs with lower PC loading. The success of using the MM-70PC fragment for BET analysis is ascribed to the lower PSf content, leaving more PBA exposed for N_2 access. Samples of MMs with PC loading higher than 70 wt% gives powders, which generate mesopores among different samples, leading to irreproducible results. Since the PBA composition is independent of the PC loading, the pore diameter of 0.54 nm (5.4 Å) in the fragment of MM-70PC is inferred to be the same as MMs with lower PC loading (10~40 wt%). Therefore, the BET measurements further support the results in PALS analysis. The PALS technique circumvents the obstruction of PBA by the PSf matrix, because it does not rely N_2 adsorption, so PALS measurements are suitable for all MMs with various PC loadings.

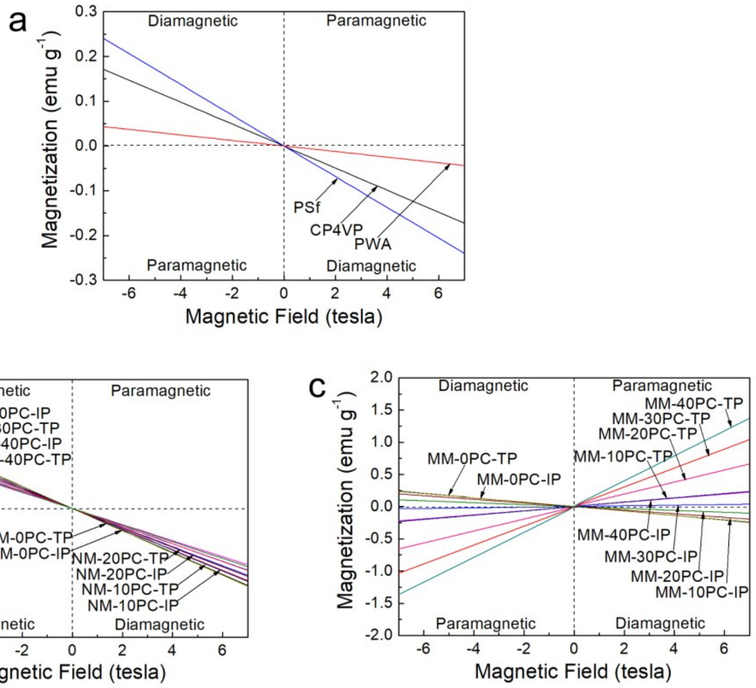

Fig. S6 Vibrating sample magnetometer (VSM) lines of (a) individual membrane components CP4VP, PWA, PSf, (b) NMs and (c) MMs at 80 ^{o}C. All individual membrane components are diamagnetic, so they cannot be aligned under magnetic field. Each NM or MM-0PC displays isotropic diamagnetism. In contrast, MMs with PC loading become strongly paramagnetic, which is due to the formation of the paramagnetic PBA framework. The VSM curves of MMs are much steeper for TP than IP, which suggests that the formed paramagnetic PBA frameworks in MMs are synchronously aligned under magnetic field.

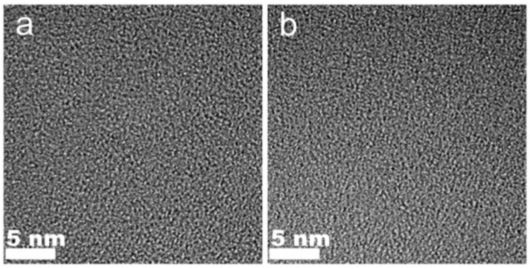

Fig. S7 Cross-sectional transmission electron microscope (TEM) images of (a) NM-0PC and (b) MM-0PC membranes. Both samples exhibit homogeneous and isotropic morphology, as the magnetic field has no influence on diamagnetic PSf.

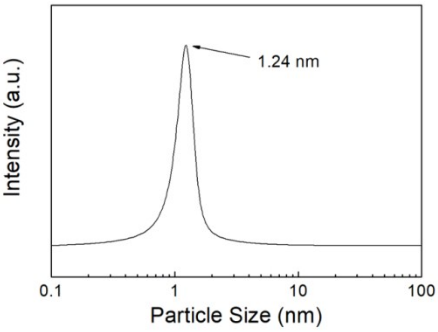

Fig. S8 PWA particle size (dispersed in benzene) estimated by the dynamic light scattering (DLS) technique. The diameter of 1.24 nm is in good accordance with the TEM observation.

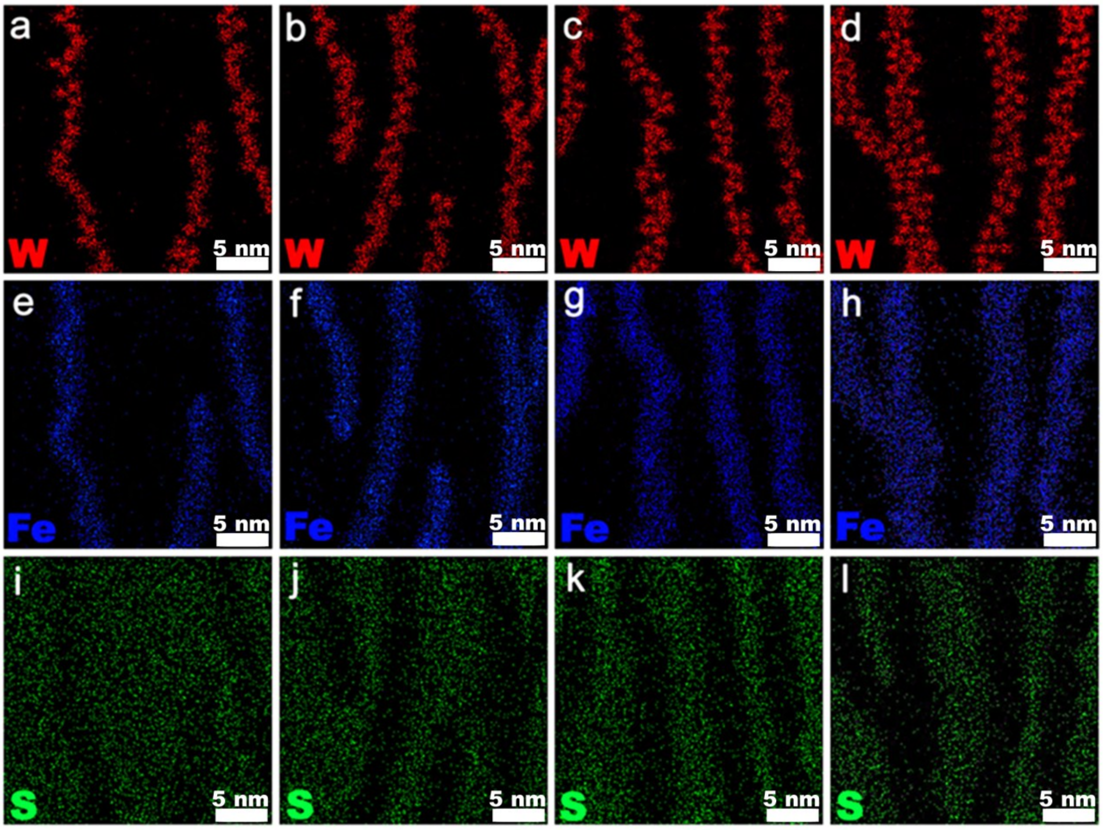

Fig. S9 (a-d) Electron energy loss spectroscopy (EELS) mapping of W in the same area of (Fig. 3e-h). (e-h) EELS mapping of Fe in the same area of (Fig. 3e-h). (i-l) EELS mapping of S in the same area of (Fig. 3e-h). The overlap of W and Fe indicates that PWA and CP4VP are closely connected after the formation of PBA. The PBA channels are embedded in the PSf matrix.

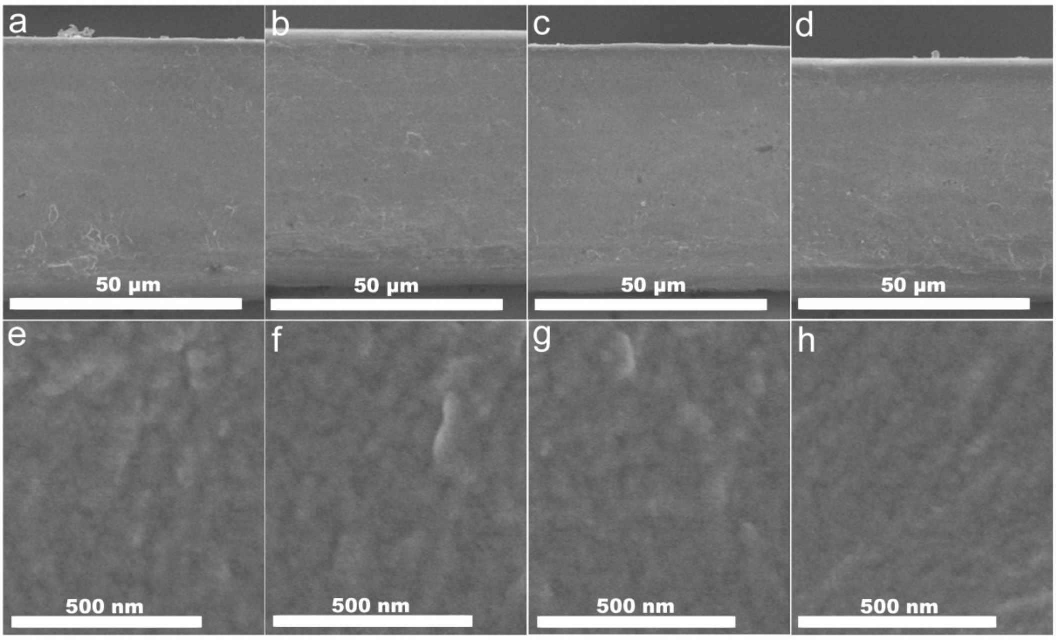

Fig. S10 Cross-sectional scanning electron microscope (SEM) images of MMs. (a-d) MM-10PC, MM-20PC, MM-30PC and MM-40PC (low magnification). (e-h) MM-10PC, MM-20PC, MM-30PC and MM-40PC (high magnification). Since the resolution of SEM is much lower than that of TEM in Fig 3, the oriented channel features are not observable in SEM images. However, Figs. S10a-d reveal that all MMs have similar thicknesses (59 μm, 57 μm, 55 μm and 54 μm for MM-10PC, MM-20PC, MM-30PC and MM-40PC, respectively), which are comparable to the 50.8 μm of Nafion® 212, ensuring the reliability of all in situ evaluations. The decreasing trend of membrane thickness with growing PC loading is attributed to the higher density of CP4VP and PWA than PSf. Moreover, Figs. S10e-h verify the uniform and dense morphology of MMs at the nano- to micro- scale, in agreement with the estimation in PALS and BET measurements that MMs contain only micropores with diameter of 5.4 Å.

Table S1 Freezable water ratio in liquid water equilibrated Nafion® 212 at 40 ^{o}C

Membrane	Integrated enthalpy in DSC from water heat of fusion ΔH_1 (J g^{-1})	Integrated enthalpy in DSC from water heat of vaporization ΔH_2 (J g^{-1})	Freezable water ratio[a] (%)
Nafion® 212	49.18	605.05	55.0

[a] Freezable water ratio (%) $= \dfrac{\dfrac{\Delta H_1}{\Delta H_\mathrm{f}}}{\dfrac{\Delta H_2}{\Delta H_\mathrm{v}}} \times 100$, where ΔH_f is the heat of fusion for bulk water (334 J g^{-1}), and ΔH_v is the heat of vaporization for bulk water (2260 J g^{-1}).

Table S2 Comparative water sorption and relative water sorption of MMs and Nafion® 212 at various RH or from liquid water at 40 °C

	Water sorption[a] (wt%)						Relative water sorption[b] (%)					
RH (%)	20	40	60	80	95	Liquid water	20	40	60	80	95	Liquid water
MM-10PC	2.4	3.4	4.3	5.3	6.3	9.3	25.8	36.6	46.2	57.0	67.7	100.0
MM-20PC	4.0	5.9	7.6	9.4	10.9	16.9	23.7	34.9	45.0	55.6	64.5	100.0
MM-30PC	7.2	10.4	13.2	16.1	19.7	29.7	24.2	35.0	44.4	54.2	66.3	100.0
MM-40PC	10.0	14.6	18.4	22.5	27.5	39.3	25.4	37.2	46.8	57.3	70.0	100.0
Nafion® 212	3.2	6.5	8.4	11.7	16.0	39.1	8.2	16.6	21.5	29.9	40.9	100.0

[a] The data at various RH were obtained by DVS test, and the data in liquid water were obtained by weight calculation, according to the method described in the “Water uptake” part of Experimental section.

[b] Relative water sorption (%) $= \dfrac{\text{Water sorption}}{\text{Water sorption in liquid water}} \times 100$

Table S3 Equilibration times of MMs and Nafion® 212 at each RH stage for the DVS test at 40 °C

	Equilibrium time[a] (min)									
RH stage (%)	0 - 20	20 - 40	40 - 60	60 - 80	80 - 95	95 - 80	80 - 60	60 - 40	40 - 20	20 - 0
MM-10PC	13.2	7.9	10.4	11.2	13.8	117.8	123.2	123.2	122.4	150.2
MM-20PC	12.4	7.8	9.9	10.8	12.8	130.8	135.4	124.7	130.7	166.1
MM-30PC	13.5	8.3	10.5	11.4	14.6	140.5	121.3	120.1	133.9	154.7
MM-40PC	13.4	8.3	10.4	11.3	14.6	151.4	131.7	130.4	145.3	167.9
Nafion® 212	18.1	24.5	24.5	34.2	39.5	35.5	32.0	20.2	36.2	31.1

[a] The DVS experiment has a parameter to determine whether the water sorption or desorption of the sample in a certain environment has achieved the equilibrium state. This parameter has a template of “less weight change of a certain wt% within a certain time”. Since membrane IEC affects the water sorption/desorption rate and amount, an impartial cross-sample comparison must be used. The equilibrium parameter in the DVS measurements is set as “less weight change of sample IEC×0.01 wt% within 30 s”. The similar overall DVS experiment periods of MMs with various PC loadings demonstrate this equilibrium parameter is largely appropriate.

Table S4 Residual water and relative residual water of MM membranes and Nafion® 212 after the DVS test at 40 °C

Membrane	Residual water (wt%)	Relative residual water[a] (%)
MM-10PC	1.3	19.8
MM-20PC	2.5	23.1
MM-30PC	3.9	19.9
MM-40PC	5.2	18.8
Nafion® 212	0.3	2.0

[a] $\text{Relative residual water (\%)} = \dfrac{\text{Residual water}}{\text{Water sorption at 95\% RH}} \times 100$

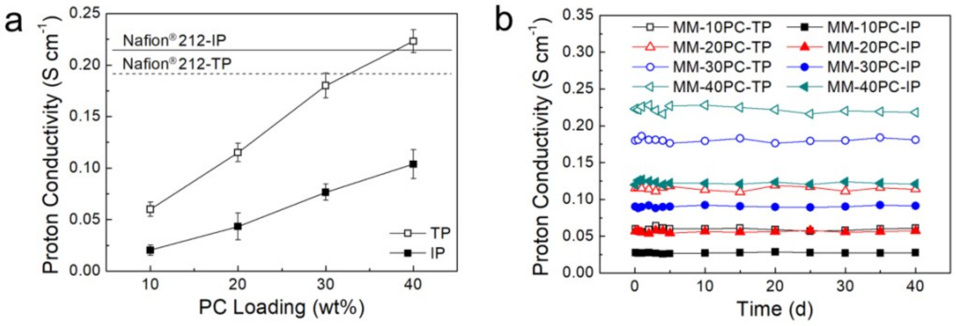

Fig. S11 (a) TP and IP proton conductivities of MMs and (b) their long-term stabilities in liquid water at 95°C. Nafion® 212 exhibits almost isotropic proton conductivity (σ_{TP} / σ_{IP} is slightly < 1), but MMs possess obviously enhanced proton conductivities in the TP direction (σ_{TP} / σ_{IP} = 2 ~ 3). Both TP and IP proton conductivities of MMs show enduring stability, indicating that the individually water-soluble CP4VP and PWA membrane components do not leach from the MMs after the formation of PBA.

Table S5 E_as for TP proton conductivity of MMs at 80% RH and 40% RH.

Membrane	E_a (kJ mol^{-1}) at 80% RH	E_a (kJ mol^{-1}) at 40% RH
MM-10PC	14.05	13.56
MM-20PC	13.37	12.85
MM-30PC	12.51	11.81
MM-40PC	11.75	11.31
Nafion® 212	17.83 (20 - 80 ^{o}C) 4.58 (80 - 120 ^{o}C)	17.37 (20 - 60 ^{o}C) 0.97 (60 - 120 ^{o}C)

Table S6 Power density relative maintenance at low RH and elevated temperature

Membrane	Maximum power density (mW cm^{-2}) (80% RH / 80 ^{o}C)	Maximum power density (mW cm^{-2}) (40% RH / 120 ^{o}C)	Relative maintenance[a] (%)
MM-10PC	257.0	150.7	58.6
MM-20PC	505.2	278.4	55.1
MM-30PC	725.5	452.0	62.3
MM-40PC	975.0	538.4	55.2
Nafion® 212	544.8	119.5	21.9

[a] $$\text{Relative maintenance (\%)} = \frac{\text{Power density at 40\% RH / 120 }^{\text{o}}\text{C}}{\text{Power density at 80\% RH / 80 }^{\text{o}}\text{C}} \times 100$$

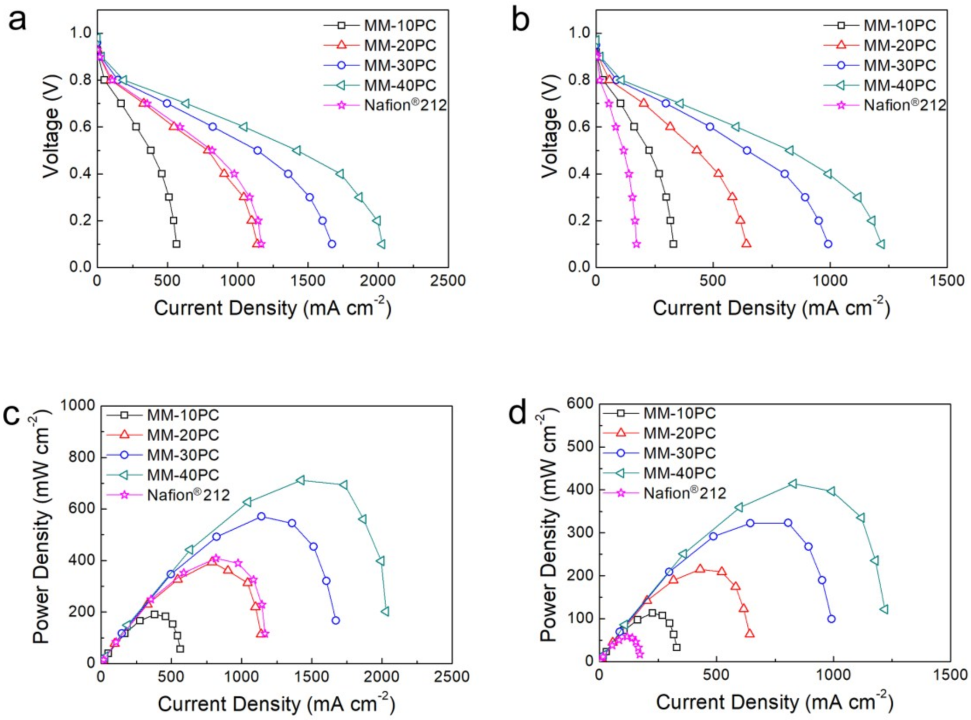

Fig. S12 Comparative H_2/air fuel cell performance of MMs and Nafion® 212 based PEMFCs. Polarization curves (a) at 80% RH / 80 °C and (b) at 40% RH / 120 °C. Power density curves (c) at 80% RH / 80 °C and (d) at 40% RH / 120 °C. At 80% RH and 80 °C, the PEMFCs based on MMs and Nafion® 212 display identical power density ratios (~ 75%) compared with H_2/O_2 operation. Under more dehydrating conditions of 40% RH and 120 °C, MM based PEMFCs still perform at similar ratios (~ 75%) as in H_2/O_2 operation, but Nafion® 212 based PEMFC shows a much greater decrease in output (~ 49%). The Pt/C loadings on anode and cathode are both 0.4 mg cm^{-2} (Pt loading 0.24 mg cm^{-2}), and H_2 and air are supplied at flow rates of 120 and 450 sccm, respectively (standard atmospheric pressure without back pressure).

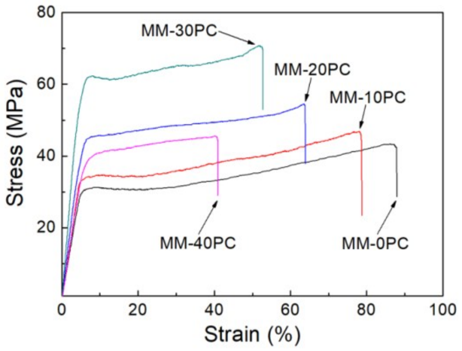

Fig. S13 Stress-strain curves of MM membranes with ASTM D882 conditions, as described in the “Mechanical properties” part in Experimental section. As PC loading increases from 0 wt% to 30 wt%, MM membranes display lower breaking elongation but higher elastic modulus and tensile strength, which is probably due to the introduction of the rigid PBA framework in PSf matrix. At a PC loading of 40 wt%, the mechanical properties show an overall deterioration because the tough PSf matrix has a relatively lower proportion to afford support. In our previous study, the mechanical properties of Nafion® 212 were also investigated[1], which are much inferior compared with any MM here.

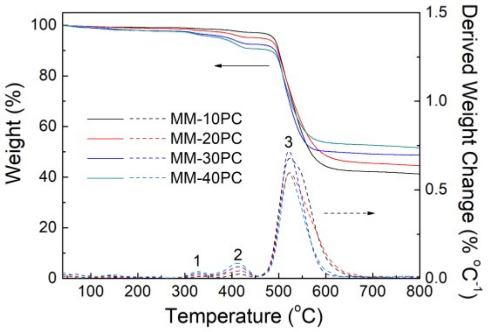

Fig. S14 Thermogravimetric analysis (TGA) measurements of MMs under N_2 atmosphere, showing weight loss and derivative weight change curves. The slight and gradual weight loss in the range of 40-200 °C is due to water evaporation, as demonstrated in DSC and DVS tests. The onset of decomposition at 325 °C occurs from the loss of C≡N groups in the PBA framework[2]. The second stage at around 412 °C derives from the main chain of CP4VP[3]. The third stage at around 521 °C is caused by the decomposition of PSf matrix[4]. The TGA results indicate that the MMs have reliable thermal stability under 300 °C.

Table S7 Comparison with reported water-retentive PEMs

Reference	Method	Membrane proton conductivity	PEMFC power density	PEMFC durability
5	External hydrophobic coating	~ 0.05 S cm^{-1} at 80 °C/100% RH	Above 1100 mW cm^{-2} at 80 °C/100% RH with H_2/O_2	10 % current density loss within 220 h at 120 ^oC/35% RH with H_2/air
6	Incorporating hydrophilic CeO_2	0.107 S cm^{-1} at 60 °C/100% RH	Above 600 mW cm^{-2} at 60 °C/75% RH with H_2/air	Rapid loss (~1.13×10^{-4} V s^{-1}) in OCV hold at 95 ^oC between dry/100% RH cycles
7	Incorporating hydrophilic TiO_2	0.155 S cm^{-1} at 80 °C/100% RH	Above 1100 mW cm^{-2} at 80 °C/100% RH with H_2/O_2	Rapid loss (1.06 mV h^{-1}) in OCV hold at 80 ^oC/100% RH with H_2/O_2
8	Incorporating hydrophilic zeolite	~0.129 S cm^{-1} at 80 °C/100% RH	510 mW cm^{-2} at 85 °C/100% RH with H_2/O_2	-
9	Incorporating Pt-based catalytic filler	0.053 S cm^{-1} at 60 ^oC/100% RH	~1430 mW cm^{-2} at 60 °C/100% RH with H_2/O_2	No obvious drop in both OCV and voltage within 100 h at 60 ^oC 800 mA/cm^2

10	Incorporating hydrophilic core–shell hybrid oxide	0.065 S cm^{-1} at 80 °C/100% RH	~ 500 mW cm^{-2} at 85 °C/50% RH with H_2/O_2	-
11	Blending polymeric capsules	~ 0.051 S cm^{-1} at 85 °C/100% RH	-	-
12	Blending double-shelled hollow spheres	0.078 S cm^{-1} at 20 ^{o}C/100% RH	-	-
13	Generating larger hydrophilic domains by solvent assistance	0.099 S cm^{-1} at 25 ^{o}C/100% RH	-	-
This work	Oriented nano-sponge PBA with 5.4 Å micropores	0.210 S cm^{-1} at 120 ^{o}C/95% RH (Through-plane)	975 mW cm^{-2} at 80 °C/80% RH with H_2/O_2	Almost no or slight current density loss in constant voltage test within 40 days at 120 ^{o}C/40% RH with H_2/O_2

Supplementary Note 3. Further discussion on the magnetic induced formation of Fe−C≡N−W PBA

Compared with the prior heteropoly blue interpretation[1], the formation of PBA is an important new finding here. Deeper investigation and new evidence suggest that the magnetically-induced interaction between CP4VP and PWA is not simple random bonding like heteropoly blue, but that there is a regular spatial arrangement where the interaction is effected on a particular W atom, establishing a covalent N−W bond, and the resulting Fe−C≡N−W structure forms a face-centered regular cubic framework having microporosity. Although some studies on heteropoly blue have reported that the transferred electron is prone to be trapped on a certain W atom, this is found only at very low temperature[14, 15], which is not the case here using ambient temperatures. We interpret some related research concerning PBA, such as changes in membrane color, solubility and magnetic transitions. Surprisingly, the PBA interpretation has the same conclusion as the heteropoly blue interpretation. It is uncommon for two independent interpretations to simultaneously and appropriately elucidate one system, so we conclude that the magnetically-induced CP4VP-PWA complex is probably at the intersection of PBA and heteropoly blue, which is valuable in these two research areas. Apart from having a microporous structure inherent with PBAs, the novel Fe−C≡N−W framework constructed by CP4VP with PWA is also hydrophilic and highly proton conductive. This is the intrinsic source of the new findings about the enhancement of water retention, together with improvements in both membrane and PEMFC performances at low RH and elevated temperature.

With the preceding characterization of the newly formed PBA framework, the color and solubility changes of MMs can be better understood. The absorbance at around 360 nm for CP4VP in the UV-Vis spectrum (Fig. S1a) is caused by the metal-to-ligand charge transfer between Fe and pyridine[16, 17], and the new absorbance at around 617 nm for MMs is ascribed to the intervalence charge transfer in the PBA framework[18, 19]. The literature reports that the absorbance of the original Fe-pyridine metal-to-ligand charge transfer shifts to a lower wavelength after the formation of PBA[16, 17], but that is not the case in the present work. Here, this is probably related to the chemically combined state of W (acting as M_2), which is less electrophilic than the reported M_2s in the cation state, thereby having an impact on the electron environment positioned only on the cyano ligand, but not around Fe-pyridine. Such inference correlates well with the results in XPS (Fig. S2a), which is also an electron-based technique, because the binding energy of the N for Fe-pyridine in MMs (after the formation of PBA) is the same as that in CP4VP. The solubility variation of MMs also derives from the formation of the Fe−C≡N−W framework, since water-insolubility is a common characteristic for similar types of PBAs that do not contain additional alkaline metal ions[20, 21].

The Fe−C≡N−W PBA shows proton conductivities of at least 2 orders of magnitude higher than any reported PBA[22], and strong water absorption, not previously encountered in any water-insoluble PBA, suggesting this type of PBA can be exploited for the fabrication of PEMs. Magnetic field inducement may also be a potential method for the construction of other types of metal organic frameworks and covalent organic frameworks which are not readily accessible under conventional conditions.

Supplementary Note 4. Further discussion on the influence by polymer matrix and solvent

Both individual casting solvents DMF and water used in the mixed solvent (5 mL DMF / 1 mL water) are diamagnetic and they were completely removed after membrane preparation, so we infer that each are not separately affected by the magnetic field, and they cannot directly facilitate the formation of the Fe−C≡N−W structure. However, we have found that the mixed solvent system, compared with DMF alone, promotes phase separation and the formation of proton channels in the magnetically-cast membranes. The polarity difference between DMF and water induces aggregation of the hydrophilic CP4VP and PWA in the water phase, resulting in better delineated proton-conducting phases.

Initial investigations of other polymer matrices were undertaken, including sulfonated poly(ether ether ketone) (SPEEK), poly(ether sulfone) (PES) and polystyrene (PS). Compared with PSf-based membranes, the membranes fabricated using the more hydrophilic SPEEK or PES showed less regulated phase separation and proton channels, while the membranes fabricated using the more hydrophobic PS displayed similarly aligned structures, but had poor mechanical strength. PSf possesses an intermediate hydrophilicity, evidently different from CP4VP and PWA, ensuring good phase separation and alignment. Furthermore, PSf is also tough to afford excellent mechanical properties. Thus, the predominately more hydrophobic and tough PSf was selected as the best matrix, and 5 mL DMF / 1 mL water was selected as the mixed solvent for membrane casting.

Supplementary References

1. X. Liu, Y. Li, J. Xue, W. Zhu, J. Zhang, Y. Yin, Y. Qin, K. Jiao, Q. Du, B. Cheng, X. Zhuang, J. Li and M. D. Guiver, *Nat. Commun.*, 2019, **10**, 842.
2. T. Kollmetz, P. Georgopanos and U. A. Handge, *Polymer*, 2017, **129**, 68-82.
3. S. J. Gerber and E. Erasmus, *Mater. Chem. Phys.*, 2018, **203**, 73-81.
4. K. Zahri, K. C. Wong, P. S. Goh and A. F. Ismail, *RSC Adv.*, 2016, **6**, 89130-89139.
5. C. H. Park, S. Y. Lee, D. S. Hwang, D. W. Shin, D. H. Cho, K. H. Lee, T. W. Kim, T. W. Kim, M. Lee, D. S. Kim, C. M. Doherty, A. W. Thornton, A. J. Hill, M. D. Guiver and Y. M. Lee, *Nature*, 2016, **532**, 480-483.
6. Z. Wang, H. Tang, H. Zhang, M. Lei, R. Chen, P. Xiao and M. Pan, *J. Membr. Sci.*, 2012, **421-422**, 201-210.
7. K. Ketpang, K. Lee and S. Shanmugam, *ACS Appl. Mater. Interfaces*, 2014, **6**, 16734-16744.
8. Y. Devrim and A. Albostan, *Int. J. Hydrogen Energy*, 2015, **40**, 15328-15335.
9. Y. Zhang, H. Zhang, C. Bi and X. Zhu, *Electrochimi. Acta*, 2008, **53**, 4096-4103.
10. V. Di Noto, M. Piga, E. Negro, G. A. Giffin, S. Polizzi and T. A. Zawodzinski, *RSC Adv.*, 2013, **3**, 18960.
11. J. Wang, H. Zhang, X. Yang, S. Jiang, W. Lv, Z. Jiang and S. Z. Qiao, *Adv. Funct. Mater.*, 2011, **21**, 971-978.
12. E. Yan, J. Wang, Z. Jiang, H. Feng, L. Nie, T. Xu, X. Yang and X. Zhang, *J.*

Mater. Chem. A, 2013, **1**, 11762.

13. X. Liu, S. He, S. Liu, H. Jia, L. Chen, B. Zhang, L. Zhang and J. Lin, *J. Membr. Sci.*, 2017, **523**, 163-172.
14. L. Ouahab, M. Bencharif, A. Mhanni, D. Pelloquin, J. F. Halet, O. Pena, J. Padiou, D. Grandjean and C. Garrigou-Lagrange, *Chem. Mater.*, 1992, **4**, 666-674.
15. C. Sanchez, J. Livage, J. P. Launay and M. Fournier, *J. Am. Chem. Soc.*, 1983, **105**, 6817-6823.
16. R. McHale, Y. Liu, N. Ghasdian, N. S. Hondow, S. Ye, Y. Lu, R. Brydson and X. Wang, *Nanoscale*, 2011, **3**, 3685-3694.
17. X. Roy, J. K.-H. Hui, M. Rabnawaz, G. Liu and M. J. MacLachlan, *Angew. Chem., Int. Ed.*, 2011, **50**, 1597–1602.
18. Y. Liu and X. Wang, *Polym. Chem.*, 2012, **3**, 2632.
19. R. Papadakis, I. Deligkiozi, M. Giorgi, B. Faure and A. Tsolomitis, *RSC Adv.*, 2016, **6**, 575-585.
20. F. S. Hegner, J. R. Galan-Mascaros and N. Lopez, *Inorg. Chem.*, 2016, **55**, 12851-12862.
21. A. K. Vipin, B. Hu and B. Fugetsu, *J. Hazard. Mater.*, 2013, **258-259**, 93-101.
22. S.-i. Ohkoshi, K. Nakagawa, K. Tomono, K. Imoto, Y. Tsunobuchi and H. Tokoro, *J. Am. Chem. Soc.*, 2010, **132**, 6620-6621.